Nano Research

Open Access

Research Article

A MXene-bridged triboelectric sensor for tinyML-empowered joint biomechanics

Guiying Wang[1,2,3,§], Xinzhi Liu[4,5,§] ✉, Yiqun Wang[4,5,§], Fuzhen Xuan[1,2,3], Bowei Zhang[1,2,3] ✉, and Xiaofeng Wang[4,5] ✉

[1] *Shanghai Key Laboratory of Intelligent Sensing and Detection Technology, East China University of Science and Technology, Shanghai 200237, China*
[2] *Key Laboratory of Pressure Systems and Safety of Ministry of Education, East China University of Science and Technology, Shanghai 200237, China*
[3] *School of Mechanical and Power Engineering, East China University of Science and Technology, Shanghai 200237, China*
[4] *Department of Precision Instrument, Tsinghua University, Beijing 100084, China*
[5] *Key Laboratory of Smart Microsystem (Ministry of Education), Tsinghua University, Beijing 100084, China*
[§] *Guiying Wang, Xinzhi Liu, and Yiqun Wang contributed equally to this work.*

Cite this article: *Nano Research*, **2026**, *19*, 94908328. https://doi.org/10.26599/NR.2026.94908328

ABSTRACT: Despite the increasing prevalence of wearable flexible sensors for human joint biomechanics, challenges, such as limited intelligence capacity, insufficient sensitivity, and power constraints, limit their practical application. To address these issues, this work presents a low-power and low-latency edge computing algorithm that incorporates interpretable machine learning to guide dimensionality reduction for direct on-sensor signal processing. Compared to traditional wireless transmission methods, the deployed tiny machine learning (tinyML) model achieves a prediction latency of only 9 ms and reduces power consumption by 75.6%. Furthermore, utilizing a triboelectric sensor based on MXene and featuring a micro-conical structure demonstrates excellent self-powered sensing capability, with output voltage and charge increased by 27.4% and 52.9%, respectively, and a high-sensitivity monitoring performance of 16 mV/Pa. The synergy between the efficient algorithm and the high-performance sensor is validated in knee joint biomechanics scenarios, showing advantages over conventional approaches in power consumption, cost, response speed, size, and accuracy. These combined strengths indicate broad application prospects in portable intelligent healthcare.

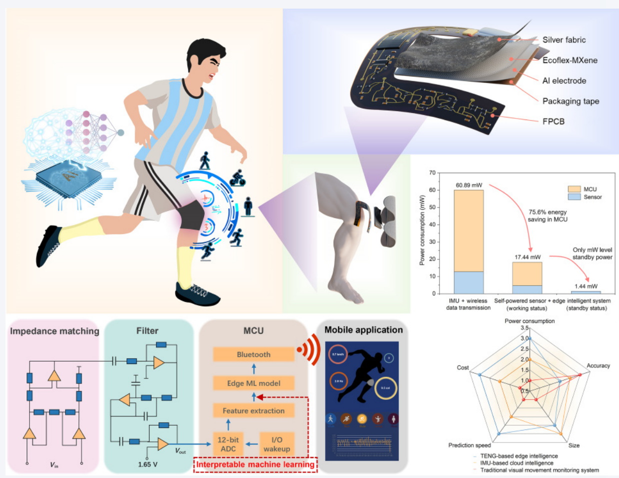

KEYWORDS: MXene, triboelectric sensor, joint biomechanics, tiny machine learning (tinyML), interpretable machine learning

1 Introduction

The monitoring, recognition [1], and evaluation of human joint biomechanics through sensors and computational models hold significant value in health management [2], medical rehabilitation [3, 4], sports training [5], and human–computer interaction [6–9]. Current solutions primarily include visual imaging systems [10, 11], inertial sensors [12, 13], and flexible electronic sensors [14–17]. Visual imaging systems capture images or videos to extract motion features with high recognition accuracy. However, they require fixed, bulky, and expensive equipment, limiting their uses. Inertial measurement units (IMUs) offer advantages in size and cost, making them more portable, but their rigid structure and poor skin adhesion, resulting from silicon-based processing, limit comfort and long-term wearability [18]. In recent years, flexible electronic sensors have gained attention due to their superior skin adhesion and biocompatibility. These sensors detect myoelectric strain or pressure signals to monitor and identify motion signals [19].

Received: October 8, 2025; **Revised:** November 27, 2025
Accepted: December 8, 2025

✉Address correspondence to Xinzhi Liu, liu-xz19@mails.tsinghua.edu.cn; Bowei Zhang, boweiz@ecust.edu.cn; Xiaofeng Wang, xfw@mail.tsinghua.edu.cn

However, practical challenges persist, including limited intelligence, insufficient sensitivity, power constraints, and a lack of real-time edge-processing capabilities. To address these issues, researchers are developing high-performance sensing systems, such as multimodal sensors with decoupled mechanisms for simultaneous measurement of pressure, strain, and temperature [20–22]; flexible pressure sensors with microstructural designs (e.g., porous or wrinkled architectures) or novel materials (e.g., liquid metals) [23–25]; and standalone flexible platforms (e.g., electronic tattoos) that enhance wearability and signal quality [26, 27]. Despite these advances, the intelligent paradigm of existing systems still faces bottlenecks.

In recent years, wearable flexible electronic sensors have been evolved to support real-time recognition systems [28, 29]. For instance, previous work reported a hierarchical triboelectric sensor based on reduced graphene oxide (rGO) for motion monitoring and trajectory tracking [30]. A biomimetic heterogeneous wettability triboelectric sensor for sweat collection and real-time monitoring has been reported [31]. However, these solutions predominantly rely on a traditional "signal sensing–wireless transmission–machine learning (ML)" paradigm, which necessitates transmitting large amounts of raw sensor data wirelessly [32, 33]. This approach is not only extremely power-hungry but may also lead to data latency and privacy issues, ultimately limiting practical applications. Despite the broad prospects of tiny ML (tinyML) technology, the comfortable and efficient integration of tinyML with high-performance flexible sensors at the hardware level remains a significant challenge, which often results in poor wearability or compromised system performance [34–36].

This study proposes a MXene-bridged triboelectric sensor for tinyML-empowered joint biomechanics. By combining material innovations (e.g., MXene-enhanced dielectric layers and micro-conical structures) and algorithm optimization (e.g., feature dimensionality reduction guided by interpretable machine learning), the system achieves high sensitivity and low power consumption. The sensor's micro-conical array ensures consistent performance under bending or stretching, improving skin conformity and output efficiency. Electrical and mechanical characterization confirms a sensitivity of 16 mV/Pa and linear response under deformation, supporting multimodal sensing. Through interpretable machine learning, feature selection optimizes model efficiency for edge deployment. The work's advantage lies not in maximizing a single parameter but in the synergy between sensor design and efficient algorithms, yielding improvements in power consumption, cost, response speed, size, and accuracy over conventional solutions [37].

2 Results and discussion

2.1 Overall configuration of the wearable triboelectric sensing system

The wearable intelligent joint biomechanics consists of a MXene-bridged triboelectric sensor and flexible printed circuit board (FPCB). Signal processing circuits and machine learning algorithms are integrated on the FPCB to realize the recognition and prediction of the wearer's movement status (Fig. 1(a)). Designed as a semi-ring structure, the FPCB positions the triboelectric sensor at its center to align with the knee joint. The lightweight, fully flexible sensor and circuit board, weighing only 6.2 grams, are wrapped in a knee pad and securely strapped to the knee joint, minimizing discomfort to the wearer (Fig. 1(b)).

The self-powered sensor operates in a contact-mode with an attached electrode triboelectric configuration (Fig. 1(c) and Figs. S1 and S2 in the Electronic Supplementary Material (ESM)), converting pressure and deformation signals into electrical signals without the need for an external power supply. The upper electrode is made of silver fabric, while the lower electrode consists of an aluminum (Al) deposition coating on the dielectric layer (scanning electron microscopy (SEM) images in Figs. S3 and S4 in the ESM). The dielectric layer is composed of Ecoflex and incorporated with MXene to improve electrical output performance (see SEM images in Figs. S5–S7 in the ESM). The elemental analysis table in Fig. S8 in the ESM using energy dispersive spectroscopy (EDS) confirms the distribution of MXene in Ecoflex. The presence of Si and Ti elements indicates the successful preparation of the MXene/Ecoflex nanocomposite (Fig. 1(e)). The silver fabric and dielectric layer form a friction pair that generates tribo-charges upon external force application (Figs. 2(a) and 2(b)).

Due to the high internal resistance (R) of the triboelectric sensor, an impedance matching circuit is utilized to achieve a low impedance input. Subsequently, a low-high-low filtering network filters out high-frequency noise, corrects low-frequency baseline drift, and stabilizes the baseline voltage at 1.65 V. Upon detection of the sensor's output, the microcontroller unit (MCU) exits standby mode and collects the signal. Once the signal is processed by the onboard circuitry and ML algorithms, the identified exercise type and related parameters, such as exercise frequency, speed, and caloric consumption, are transmitted to the mobile application via onboard Bluetooth, achieving real-time movement recognition and visualization on the mobile terminal (Fig. 1(d)).

2.2 MXene-bridged triboelectric sensor design with good skin compliance

Unlike traditional flat-panel sensors, monitoring knee joint biomechanics requires flexible sensors that conform to the knee's contour while maintaining high sensitivity and avoiding errors caused by varying skin topography. To address this, we designed a sensor incorporating micro-conical structures in the friction layer to enhance elasticity and reinforced the dielectric layer with $Ti_3C_2T_x$ MXene (Fig. 2(a) and Fig. S12 in the ESM). Under external force, the conductive fabric contacts the dielectric layer, generating triboelectric charges; upon force removal, the micro-cones' elasticity ensures rapid rebound. Finite element simulations illustrate changes in potential distribution during the sensor's operational cycle (Fig. 2(b) and Fig. S13 in the ESM). Our prior work confirmed that the micro-conical structure enables prompt shape recovery after pressure release, ensuring sufficient bandwidth and enhanced output.

$Ti_3C_2T_x$ MXene, a novel two-dimensional material with excellent conductivity and electronegativity, serves a dual role when incorporated into the dielectric layer [38, 39] (oxidation behavior discussed in Note S1 in the ESM). Simulation results indicate that adding MXene flakes significantly increases the sensor's output voltage and equivalent capacitance (Figs. 2(c) and 2(d)). Experimental data show a voltage increase from 48.2 to 61.4 V (27.4% growth), while simulations reveal a rise from 48.4 to 61.7 V (27.5% growth), demonstrating close agreement (Fig. S14 in the ESM). Mechanistically, MXene acts as a conductor, effectively reducing the dielectric layer's thickness and increasing capacitance,

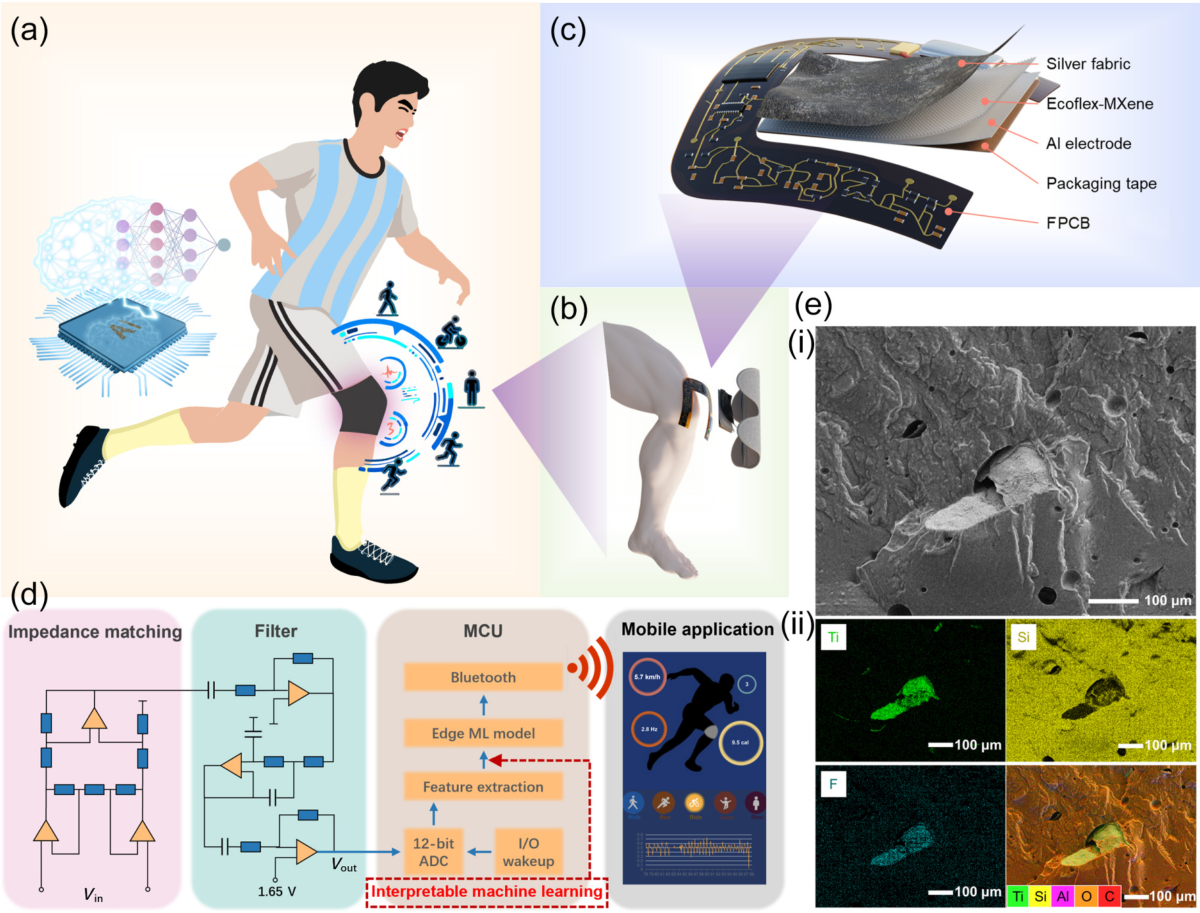

Figure 1 Overall configuration of the wearable system. (a) Schematics of the proposed wearable intelligent knee pads with tinyML. (b) Structural diagram of flexible triboelectric sensor and circuit board. (c) Hierarchical structure diagram of wearable knee pads. (d) Signal processing schematic diagram of wearable intelligent knee pads with tinyML, consisting of four parts: impedance matching, filtering, MCU processing, and mobile application. (e) (i) SEM image of the triboelectric sensor showing the cross-section of the Ecoflex-MXene dielectric layer with embedded MXene flakes and (ii) elemental EDS mapping of the Ecoflex-MXene dielectric layer with embedded MXene flakes.

thereby enhancing charge transfer during contact–separation cycles. Simultaneously, it boosts the dielectric layer's electronegativity, attracting more triboelectric charges and increasing surface charge density and output voltage, which directly improves open-circuit voltage (V_{oc}) and short-circuit charge (Q_{sc}) (Figs. S14 and S15 in the ESM). Theoretical analyses, finite element simulations (Note S2 in the ESM), and experimental results (Fig. 2(k)) corroborate these effects. The micro-conical structure alone increased output voltage and charge by 217% and 319%, respectively. MXene incorporation further elevated these values to 61.4 V and 219.1 nC, representing additional gains of 27.4% in voltage and 52.9% in charge (Fig. 2(k)). The sensor exhibited excellent durability, with negligible output degradation after 10,000 reciprocating cycles over 165 min (Fig. 2(e)). Recent extended tests (over 350,000 pressure cycles) confirmed sustained performance, underscoring long-term stability (Fig. S16 in the ESM). Five sensor batches fabricated identically showed consistent linear responses with acceptable inter-batch variability (Figs. S17 and S18 in the ESM). Environmental tests revealed stable output within 20%–80% relative humidity (RH) and −5–35 °C; detectable signals persisted even at 100%–110% RH, ensuring reliability in daily use (Fig. S19 in the ESM).

Notably, the micro-conical structure ensures consistent electrode spacing even when the sensor is bent or stretched, enhancing skin compliance (Note S3 and Figs. S20 and S21 in the ESM). This design physically isolates sensitivity mechanisms for different signals, reducing cross-talk. We further evaluated the sensor's adaptability under dynamic impedance matching scenarios (Fig. S22 in the ESM). Experiments have confirmed that voltage changes occur only under applied pressure. The amplitude and frequency of raw signal waveforms vary under different exercise intensities. As observed from the distribution diagrams, each type of movement exhibits a wide speed range, which provides diverse training data for the speed prediction of the tinyML model and enhances the model's generalization ability in dynamic scenarios (Figs. S23 and S24 in the ESM). In addition, we assessed the sensor's output under various external forces in different shapes (Figs. 2(f)–2(h) and 2(l)), and the raw data graphs are shown in Figs. S25–S27 in the ESM. In a flat state under pressure (Fig. 2(f)), the sensor exhibits linearity up to 700 g with a sensitivity of 16 mV/Pa. When simulating the knee's curvature by attaching the sensor to a cylindrical base (Figs. 2(g) and 2(i)), voltage output remained unchanged, indicating unaffected sensitivity. Besides, a 50% stretch reduces the dielectric layer's modulus (Fig. 2(h)), slightly decreasing the electrode rebound and output voltage but maintaining linearity within the operational range. It is obvious that after the sensor is stretched, the spacing of the micro-cone structure increases and the density decreases (Fig. 2(j)), lowering

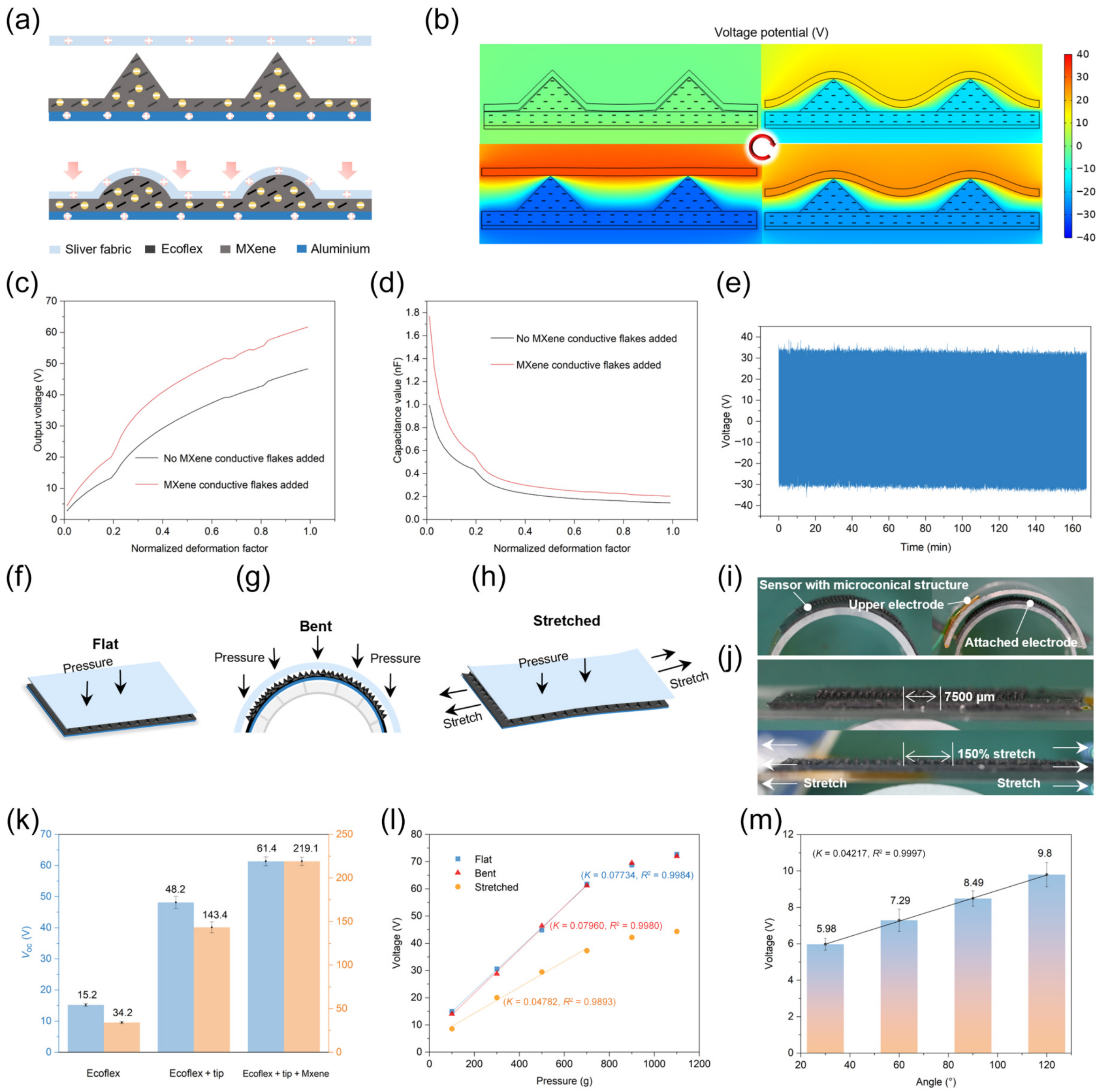

Figure 2 Electrical and mechanical characterizations of the MXene-bridged triboelectric sensor. (a) Schematic diagram of working principle. (b) Simulated sensor output potential distribution by COMSOL. (c) The variation curve of the simulated output voltage of the triboelectric sensor before and after adding MXene conductive flakes. (d) The variation curve of the simulated capacitance of triboelectric sensor before and after adding MXene conductive flakes. (e) The output signal of the sensor working for a long time. ((f)–(h)) Schematic illustrations of the sensor operating under (f) original, (g) bent, and (h) stretched states. (i) Images of the experimental device for pressure testing under the slightly bent state of the sensor. (j) Images of the experimental device for pressure testing under the stretched state of the sensor. (k) Comparison of the output performance (V_{oc} denotes open-circuit voltage and Q_{sc} denotes short-circuit charge) of three sensors, including the original flat-plate triboelectric sensor, the sensor with micro-cone structures, and the sensor adding MXene. (l) Output voltage after applying different pressure to the sensor when it is in flat, bent, or stretched states. (m) Output voltage of the sensor at different angles when attached to the joint.

sensitivity marginally while preserving functionality. Thus, signal independence enables algorithmic decoupling. It is possible for the proposed sensor to measure the knee joint bending angle (Fig. 2(m) and Fig. S28 in the ESM). When the joint bending angle gradually increases, the sensor output voltage also increases, and the sensitivity is 42 mV/°.

2.3 Interpretable machine learning analysis and model deployment for knee motion

It is a common practice to directly analyze the sensing signals of wearable devices using deep learning methods (such as convolutional neural network (CNN) and long short-term memory network (LSTM)) [39–41]. However, this approach is not ideal for tinyML wearable devices due to potential computing power and power consumption limitations, as well as the risk of overfitting from limited data. In contrast, physiological electrical signal research often employs simple ML models after feature extraction from raw signals. This practice is less common in movement monitoring due to the difficulty of extracting physically meaningful indicators from knee joint motion signals. Here, we utilize interpretable ML methods to analyze the time-frequency domain characteristics of knee joint motion signals. This approach guides dimensionality reduction and selects a subset of features with clear physical meanings for deploying edge-end ML models (Fig. 3).

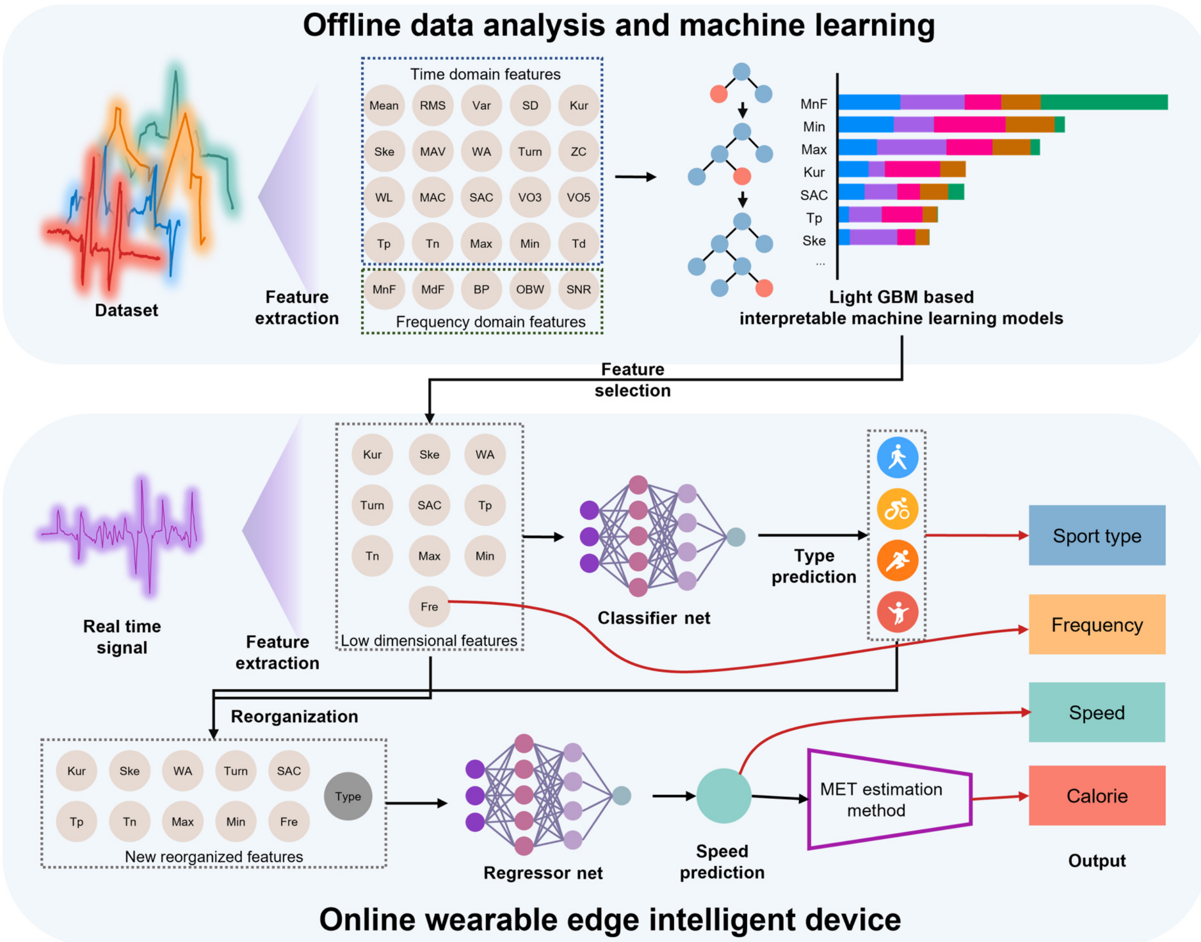

Figure 3 Diagram of interpretable machine learning analysis and machine learning model deployment. The process consists of two main parts. First, an offline interpretable ML model analysis is conducted using the SHAP method, which trains on 25 time and frequency domain features extracted from the original data. This analysis assesses the contribution of each feature, leading to the identification of 10 key features with clear physical significance for real-time intelligent motion monitoring. Second, an online wearable tinyML model is deployed, comprising networks for classifying motion types and predicting motion speed. They are all pre-trained and deployed on wearable edge devices. The motion detection analysis results, encompassing motion type, frequency, speed, and calorie consumption, are transmitted to a mobile application via Bluetooth. For further details on the network structure, mobile application, and the metabolic equivalent (MET) calculation method for determining calorie expenditure, refer to Section 4 and Note S8 in the ESM.

For the original motion signal of the knee joint, 25 representative indicators were selected for feature extraction, encompassing time-domain statistics, signal shape descriptors, and spectral data (Note S4 in the ESM). Shapley additive explanation (SHAP) is a game-theoretic approach to explain the output of almost any ML model. Here, light gradient boosting machine (GBM) serves as interpretable ML model to visualize the contribution of each feature to the prediction results. By employing this interpretable ML method, we demystified the motion monitoring intelligent model, revealing its internal workings and making it transparent rather than being a “black box”.

The front-end sensor provides a physical foundation for data decoupling, while the back-end establishes a direct mapping between composite signals and the target state through ML algorithms and calibration. Voltage waveforms captured over a fixed period for five motion types exhibit distinct characteristics (Fig. S29 in the ESM). Violin plots of SHAP values illustrate the contribution of each of the 25 features to motion classification (Fig. 4(a)). Interpretable ML analysis reveals that features like kurtosis (Kur) and skewness (Ske) contribute differently across motions (Note S5 in the ESM). The intensity of the color represents the value of the feature, while the positive or negative SHAP value represents whether feature makes the sample easier or more difficult to identify as this type of motion. The cumulative contribution of each feature is detailed in Fig. S30 in the ESM. Notably, Features 17 (time exceeding negative thresholds (Tn)) and 19 (minimum value (Min)) significantly positively impact walking classification (Fig. 4(a)(i)). During walking, legs remain largely upright with minimal muscle stretching, resulting in reduced sensor force and more negative waveform patterns. For running, Features 5 (kurtosis) and 18 (maximum value (Max)) have strong negative impacts, whereas Features 9 (peak turning point count (Turn)) and 19 contribute positively (Fig. 4(a)(ii)). This is because knee bending during running is confined to a specific angle range, producing flatter signal peaks, while higher muscle contraction frequency yields more subtle peaks. These findings link model decisions to joint biomechanics reality.

Some features can clearly distinguish between multiple sports. Different significant contributions of features corresponding to different motions (Fig. S31 in the ESM). For instance, Feature 6 (skewness) exhibits markedly different SHAP values in cycling compared to the previous two sports, closely related to the change

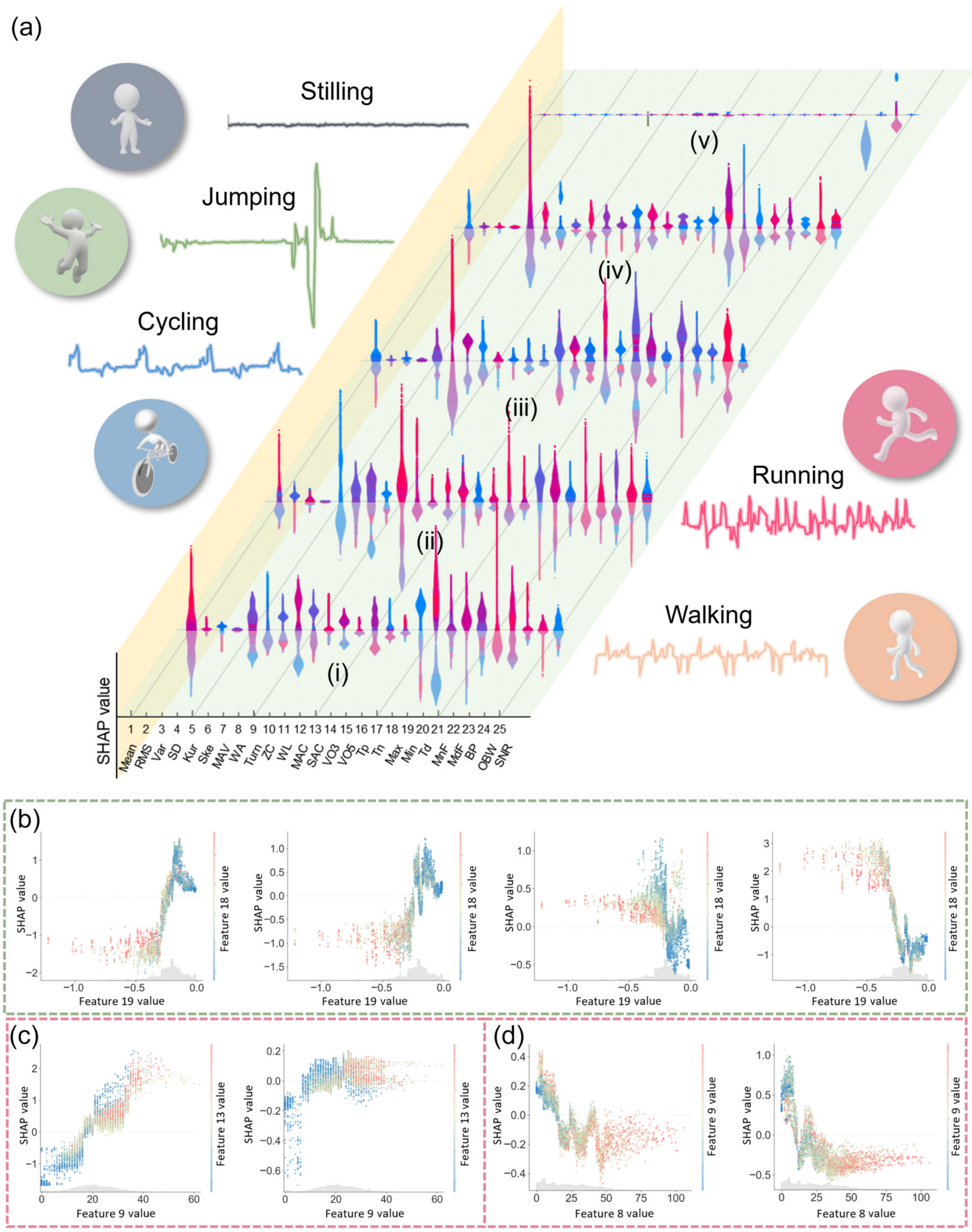

Figure 4 Feature importance analysis of five types of movements (walking, running, cycling, jumping, and stilling). (a) Violin plot of the 25-dimensional feature SHAP values for five action types displayed in waterfall format, with colors indicating the values of the input features. A higher SHAP value indicates a greater positive contribution to the classification of the sample into its respective category. Conversely, a lower SHAP value suggests a negative contribution, implying that the sample is less likely to be classified into that category. (b) Scatter plot of SHAP values when Features 18 and 19 change in the first four types of movement. (c) Scatter plot of SHAP values when Features 9 and 13 change in running and cycling movement. (d) Scatter plot of SHAP values when Features 8 and 9 change in running and cycling movement.

in knee angle during a pedaling cycle. This is due to the knee angle's transition from minimum (when the pedal is at the 6 o'clock position) to maximum (when the pedal is at the 3 o'clock position) within just one-fourth of the pedaling cycle (Fig. 4(a)(iii)). Additionally, kurtosis is crucial for differentiating between jumping and running. In the case of jumping, kurtosis positively impacts the ML model because the significant force exerted on the knees results in a sharper peak shape (Fig. 4(a)(iv)). Finally, spectral features, such as mean frequency, median frequency (Fre), and signal occupancy bandwidth, effectively distinguish among the four types of movements and a resting state. During rest, the subject's dominant frequency is approximately 0 (Fig. 4(a)(v)), with the knees essentially not exerting force, leading to a narrow frequency spectrum. Detailed results of interpretable ML analysis on 25 features can be found in Note S6 in the ESM.

Model decisions often rely on feature interactions. Beyond individual feature interpretability, we studied feature correlations via scatter plots of their SHAP values (Figs. 4(b)–4(d)). As can be seen from the definition of the features, Features 18 and 19 both reflect the extreme values of motion, and they have opposite contributions to the four types of motion except for stilling: Feature 19 has a significant positive impact on the first two types and a significant negative impact on the last two types; while Feature 18 is the opposite (Fig. 4(b)). The potential correlation between two features can be further explored. For example, for two periodic sports that are easy to confuse, such as running and cycling, as a feature that provides some additional information about the frequency performance of the signal, Feature 9 shows obvious positive correlation, but a larger Feature 13 value will reduce or increase the absolute value of SHAP (Fig. 4(c)). However, the positive contribution of Feature 9 is not absolute. For example, Feature 8 shows a relatively obvious negative correlation contribution, and the waveform complexity of running is definitely higher than that of cycling. Therefore, a smaller Feature 9 value will significantly reduce the SHAP value of running and increase the SHAP value of cycling (Fig. 4(d)).

To further optimize the model for edge device deployment, we systematically performed feature selection and hyperparameter tuning (Note S7 and Fig. S32 in the ESM). Following above analysis, feature selection identified the 10 feature dimensions—Kur (Feature 5), Ske (Feature 6), Willison amplitude count (WA, Feature 8), Turn (Feature 9), standard deviation of mean amplitude changes (SAC, Feature 13), time exceeding the positive thresholds (Tp) and Tn (Features 16 and 17), Max and Min (Features 18 and 19), and Fre—as having the most significant impact on the model. These findings align with results from feature screening using random forests or gradient boosting methods (Fig. S33 in the ESM). The SHAP mean absolute value reflects the average influence of these features on the five movement types (Fig. S34 in the ESM), and the SHAP analysis results for the ten feature dimensions post-feature screening are presented in Fig. S35 in the ESM.

We evaluated the model's performance by comparing the 25-dimensional raw features of the collected motion data with the 10-dimensional features after feature selection. The comparison was visualized using a confusion matrix. The model achieved an accuracy of 98.8% before feature selection (Fig. 5(a)) and maintained a high accuracy of 98.3% after feature selection (Fig. 5(b)). Reducing the dimensionality of the features decreases the computational and storage requirements, thereby improving the model's efficiency and speed, which is crucial for deploying models on embedded devices.

The speed distribution for walking, running, and cycling remained consistent after feature extraction, indicating that the process does not significantly affect the overall speed distribution. For these activities, the mean absolute percentage error (MAPE) of the speed estimate was 2.24% before and 2.17% after feature extraction, and the root mean square error (RMSE) was 0.544 km/h before and 0.546 km/h after feature extraction (Figs. 5(c)–5(e)). The speed prediction results for the three activities demonstrate that the model's predictive performance remains excellent after feature selection. This further illustrates that the interpretable ML analysis method, which guides dimensionality reduction, can effectively enhance the model's ability to identify key features. By focusing on the most important features, the model's generalization ability is

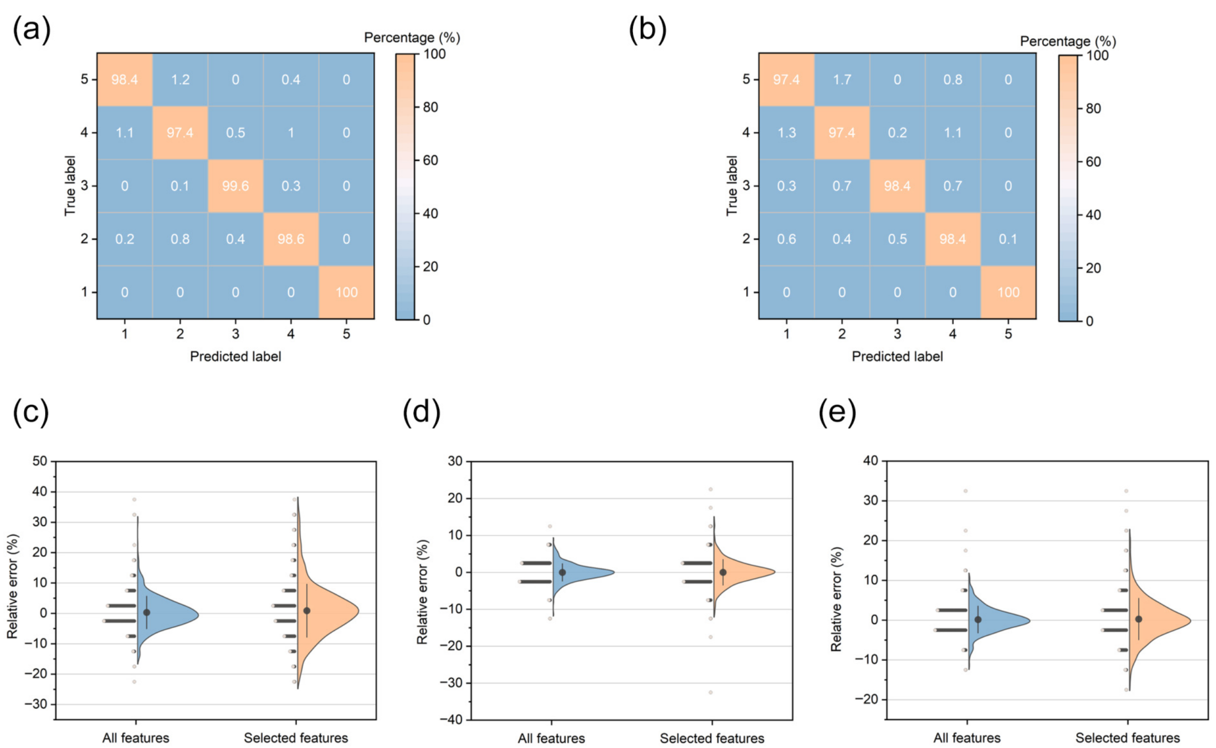

Figure 5 (a) Machine learning results before feature selection. (b) Machine learning results after feature selection. (c) Comparison of data distribution for speed prediction before and after feature selection under walking condition. (d) Comparison of data distribution for speed prediction before and after feature selection under running condition. (e) Comparison of data distribution for speed prediction before and after feature selection under cycling condition.

improved, making it better suited for real-world applications on edge devices.

2.4 Application of tinyML-empowered joint biomechanics monitoring system

To verify the effectiveness of the proposed wearable joint biomechanics system, subjects were invited to participate in practical testing wearing the system (Fig. 6(a)). During exercise, the system monitored subjects' knee joint movements in real time and identified five action categories: walking, running, cycling, jumping, and standing still. Additionally, the system predicted exercise frequency, energy consumption, and movement speed for walking, running, and cycling. These prediction results were sent to a mobile application in real time via Bluetooth (Fig. 6(b) and Note S9 and Movies S1–S3 in the ESM). A confusion matrix displayed the classification and recognition results, achieving a total accuracy of 89.1% (Fig. 6(c)). A violin plot presented the speed prediction results for three of the movements, with the MAPE of the speed estimate being 8.9%, and the RMSE being 1.11 km/h (Fig. 6(d)).

Compared with IMU-based cloud intelligent system and

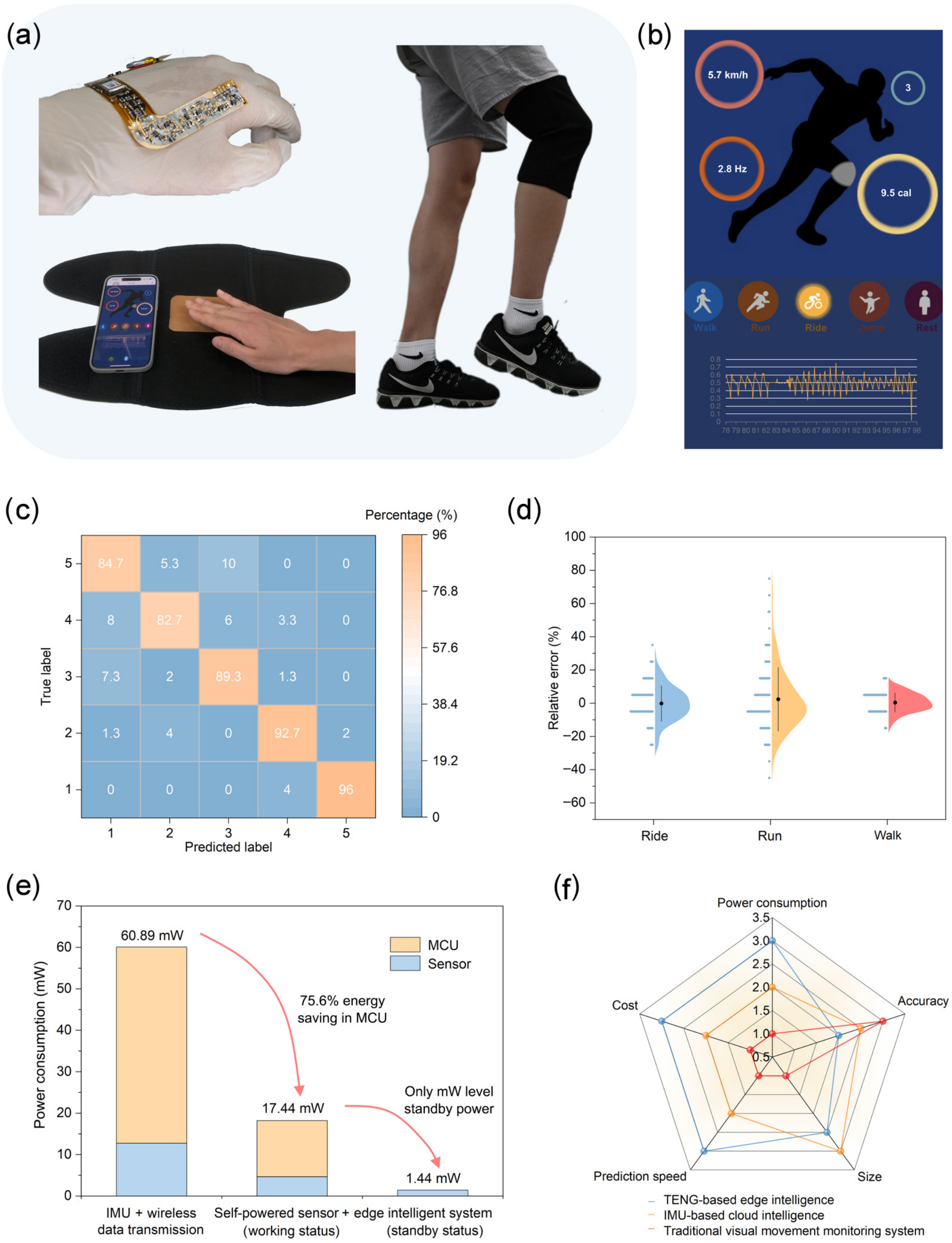

Figure 6 Practical application evaluation of MXene-bridged Triboelectric Sensor for tinyML-empowered joint biomechanics. (a) Photos of FPCB, wearable kneepad, and user wearing. (b) Mobile application user interface diagram. (c) Confusion matrix plot of motion classification results. (d) Violin plot for motion velocity prediction. (e) Comparison of power consumption of wireless data transmission scheme and the proposed self-powered sensor combined with tinyML system scheme. (f) Radar chart for performance qualitative comparison of self-powered tinyML system, IMU-based cloud intelligent system, and traditional visual movement monitoring system.

traditional visual movement monitoring system, the proposed self-powered tinyML sensing system has significant advantages in power consumption, cost, prediction speed and size. Transmitting raw information wirelessly to the cloud for analysis would increase power consumption to 47.36 mW. However, under the tinyML real-time monitoring system, the MCU's power consumption is only 12.74 mW during operation, reducing power consumption by 75.6% compared to wireless transmission (see power consumption evaluation in Section 4 and Note S6 in the ESM). Further, considering that the proposed triboelectric sensor is self-powered, the system only consumes 4.7 mW for the sensor signal processing circuit and achieves standby power as low as 1.44 mW, which is less than active motion sensors (for example, the average operating power consumption of MPU6050 and LSM9DS is 13.5 and 15.2 mW respectively, which are one of the most common commercial micro-IMUs nowadays) (Fig. 6(e)). Furthermore, since the triboelectric sensor is self-powered, the system only consumes 4.7 mW for signal conditioning, with a standby power as low as 1.44 mW. This is lower than active motion sensors, such as the MPU6050 (13.5 mW) and LSM9DS1 (15.2 mW), which are commonly used commercial micro-IMUs (Fig. 6(e)). The entire system (sensor and FPCB) weighs only 6.2 grams and achieves fully flexible and highly integrated sensing–processing–communication functionality. It offers superior wearability compared to systems based on rigid IMUs or external circuitry (Table S1 in the ESM). To further verify the clinical applicability of the proposed system, we conducted a systematic benchmark test against mainstream IMU solutions (see Table S2 in the ESM). Although the accuracy of this system is slightly lower than that of some IMU solutions, it exhibits outstanding performance in terms of cost, prediction speed, and overall power consumption. The circuit cost is below 100 RMB (approximately 14 USD), and the tinyML model delivers inference within 9 ms. Unlike many existing tinyML applications, this study integrates self-powered sensing with interpretable, low-power edge intelligence, providing an end-to-end solution for joint biomechanics monitoring (Table S3 in the ESM). As summarized in the radar chart (Fig. 6(f)), the proposed system outperforms or matches alternative solutions across multiple metrics, indicating strong potential for portable health monitoring (with the direction “higher is better” indicating ideal performance). Table S2 in the ESM offers a multi-dimensional comparison between the proposed system, typical IMU solutions, and traditional visual motion monitoring systems, covering sensing mechanisms, performance metrics, system integration, and applicability. This work presents the first integration of an MXene-bridged triboelectric sensor with a tinyML framework. The synergy between the high-performance sensor and energy-efficient algorithm enables advantages over conventional systems in power consumption, cost, response speed, size, and accuracy. Future work will focus on further optimizing the neural network and expanding the dataset to achieve even higher recognition accuracy (Table S6 in the ESM).

3 Conclusions

This study presents a MXene-bridged triboelectric sensor system for tinyML-enabled joint biomechanics monitoring. The system achieves fully flexible integration of the sensing unit and signal processing module. We first employed an interpretable machine learning framework to analyze the time-frequency characteristics of knee joint motion signals. This analysis guided feature dimensionality reduction, resulting in a compact yet discriminative feature set for model input, thereby ensuring both efficiency and reliability of the deployed tinyML model. The optimized model was subsequently deployed on a low-power edge device, enabling energy-efficient system operation (Table S4 in the ESM). Corresponding software was developed to receive and display intelligent analysis results in real time. In terms of sensor design, a unique micro-conical array structure was fabricated on the surface of the tribological layer. This design ensures conformal contact with human skin and enables high-sensitivity motion monitoring. Furthermore, incorporating MXene into the Ecoflex friction layer significantly enhanced charge trapping capability and surface charge density, leading to excellent self-powered sensing performance. The primary advantage of this work lies not in maximizing a single performance metric, but in the synergistic integration of high-performance sensing with ultra-low-power edge intelligence (Table S5 in the ESM). The underlying mechanisms of the structural and material innovations were elucidated through detailed simulation modeling. The system's high recognition accuracy was experimentally validated through knee joint monitoring tasks. Compared with other sensing systems, the synergy between the efficient algorithm and the high-performance sensor shows advantages over conventional approaches in terms of power consumption, cost, response speed, size, and accuracy. The work of this study embodies the interdisciplinary integration of materials science, electronic circuit design, and interpretable tinyML, providing support for the development of the wearable health monitoring field.

4 Method

4.1 Fabrication of MXene-elastomer composite dielectric layer and triboelectric sensor

A MXene-reinforced elastic dielectric layer featuring a surface micro-conical array was fabricated through a multi-step process, as illustrated in Figs. S3–S7 and S9–S11 in the ESM). First, 3.2 g of lithium fluoride (LiF) was dissolved in 80 mL of hydrochloric acid (HCl) solution under continuous stirring within a constant-temperature water bath maintained at 35 °C. After 15 min, ensuring complete dissolution of LiF, 1 g of titanium aluminum carbide (Ti_3AlC_2) powder was gradually added to the mixture. The reaction proceeded under continuous stirring at 35 °C for 48 h. Upon completion of the reaction, the mixture was aliquoted into centrifuge tubes (80 mL per tube) and subjected to a series of washing and centrifugation steps. Initially, the product was washed twice with 1 mol/L HCl to remove excess LiF. This was followed by multiple cycles of washing with deionized water and centrifugation at 3500 rpm for 5 min per cycle. The washing-centrifugation process was repeated 4–6 times until the supernatant reached a pH greater than 6. The resulting precipitate was then subjected to ultrasonication for 30 min. Finally, the product was collected and dried in a vacuum oven at 60 °C for 12 h, yielding the final MXene powder.

For the preparation of the dielectric layer, 1 g of the as-synthesized MXene powder was dispersed in 30 mL of absolute ethanol and treated with ultrasonication for 30 min to obtain a homogeneous MXene dispersion. This dispersion was then mixed with an uncured Ecoflex 00-30 precursor (in a 1A:1B ratio, where Component A is epoxy resin and Component B is curing agent). The resulting mixture was poured into a mold featuring a micro-conical array (parameters: depth 500 μm, base radius 500 μm, and array spacing 1500 μm). The mold was placed in a vacuum desiccator for degassing, facilitating the infusion of the MXene-Ecoflex mixture into the micro-conical cavities (the specific function of this structure is demonstrated in Fig. S36 in the ESM). Subsequently, the mold was transferred to a spin coater. The spin-coating parameters were set as 300 rpm for 10 s, followed by 550 rpm for 45 s. Curing was achieved through a stepwise temperature increase from 50 to 120 °C, with 30 min intervals at each 10 °C increment. Finally, the fully cured MXene-reinforced elastic dielectric layer with the micro-conical surface structure was demolded.

The surface structure of the micro-cone array was fabricated on a SiO_2 substrate using ultrashort pulse laser processing equipment (Inducer-6001-P, DelphiLaser). Each micro-cone has a depth of 500 μm, a base radius of 500 μm, and an array spacing of 1500 μm (Figs. S9 and S10 in the ESM). To facilitate demoulding, a silicone mold release agent (E206, Stoner) was applied before pouring the MXene-Ecoflex mixture. A 250 nm thick Al layer was deposited on the back side of the dielectric layer as the bottom electrode. Fabric soaked with conductive silver paste served as top electrode (Fig. S3 in the ESM). The entire triboelectric sensor, along with the FPCB, was fixed to a commercial knee pad with a water-absorbent and breathable 3M dressing to form a wearable sports monitoring system.

4.2 Finite element simulation

The changes in electric potential field distribution of the triboelectric sensor during its working cycle were determined using the finite element simulation software COMSOL 6.1. The parameters of electrode materials silver (Ag) and Al were based on COMSOL's built-in parameters. The relative dielectric constants of Ecoflex and MXene were set at 11.7 and 89, respectively. The surface charge density of the dielectric layer was specified as 1.75 $\mu C/m^2$. To simplify the simulation, a two-dimensional model was chosen, focusing on two micro-cones as the simulation units. The deformation process of the upper electrode under pressure was simulated using a parameterized deformation curve.

To assess the impact of adding MXene material on the electrical output performance (Note S2 in the ESM), the MXene flake was modeled as a conductive terminal. This setup verifies that the incorporation of MXene material enhanced the output efficiency of the triboelectric transducer. Additionally, an extra surface charge density of 0.5 $\mu C/m^2$ was applied to the surface of the MXene to evaluate the resulting increase in output voltage.

4.3 Circuit design of wearable device

FPCB incorporates four modules: impedance matching, filtering, MCU, and energy management (Figs. S37–S40 in the ESM). The equivalent circuit diagram is depicted in Fig. S41 in the ESM, which was designed according to Fig. 1(d).

The triboelectric sensor's internal resistance was at the MΩ level, and its output current was at the μA level, making it incompatible for direct sampling by the analog-to-digital converter (ADC). Operational amplifiers with low input bias current (OPA705, input bias current = 1 pA) were utilized to create a differential amplification circuit for impedance matching. The amplification factor (K) was calculated using Eq. (1)

$$K = \frac{R_2}{R_1 + R_2 + R_3} \frac{R_4 + R_5 + R_6}{R_5} \tag{1}$$

where R_1, R_2, and R_3 have larger resistances of MΩ level, preventing the friction voltage from exceeding the operational amplifier's working range, and R_4, R_5, and R_6 have resistances at the kΩ level, used to adjust the differential amplification factor.

The filter module comprises two high-pass filters and a low-pass filter. The first is an inverse high-pass filter for correcting the sensor's baseline voltage drift, with a cutoff frequency of 0.1 Hz. The second is a second-order Sallen–Key low-pass filter designed to eliminate high-frequency noise and power-line interference. The cutoff frequency (f_c) was calculated using Eq. (2)

$$f_c = \frac{1}{2\sqrt{R_{13}R_{14}C_2C_3}} \tag{2}$$

where f_c = 29.69 Hz. In practical design, C_2 and C_3 are usually simplified as $C_2 = C_3$ so as to select an appropriate capacitance value. The third is a high-pass filter with voltage bias and a cutoff frequency of 0.1 Hz. Considering that the operating voltage rail of the MCU is 0 to 3.3 V, this filter can bias the signal to 1.65 V to prevent negative voltage signals from being cut off. The circuit design ensures the readability of high internal resistance signals through an impedance-matching and filtering network, providing a stable front-end for different exercise intensities.

The Nina-B306 low-power module was employed for system control, signal processing, and wireless communication. It features a powerful ARM Cortex M4 computing chip (nRF52840), low-power Bluetooth 5, and an onboard antenna. Programs for power management, signal sampling, feature extraction, wireless communication, and tinyML models are deployed in the MCU using a J-link writer.

The energy management module includes a low-leakage rectifier bridge for self-powered sensor wake-up and a low-noise positive and negative voltage rails integrated regulator (LM27762). This voltage regulator provides both positive and negative 3.3 V voltages for chip power supply and reference voltage rails for signal processing circuits.

4.4 Pre-training and deployment of tiny machine learning models

The proposed wearable system was worn by subjects on their knee joints, continuously collecting movement waveforms, and dividing them into 4 s samples for training. Walking and running samples were collected on a treadmill, and the cycling samples were obtained on a spin bike. The samples were transmitted to a computer via Bluetooth on the FPCB for analysis and training. Interpretable ML analysis was conducted in a Python 3.8 environment using the open-source SHAP library. The feature extraction algorithm was tested in Matlab 2022b and deployed on the MCU using the built-in C Coder plug-in. The tinyML model was trained on the Edge Impulse platform, which is an open platform for developing, deploying, and scaling embedded ML applications on edge devices. A 5-layer ML model with a dropout layer was constructed and built as a native library callable by the MCU main program. According to the Edge Impulse platform's simulation results, the tinyML model operates at a 32-bit floating-point precision in 9 ms and occupies 1.5 kB of random access memory (RAM) and 15.9 kB of flash. The model optimization process comprises two key steps: feature selection and hyperparameter tuning. Based on the results of SHAP analysis, feature selection filters out 10-dimensional core features (such as kurtosis, skewness, etc.) from the 25-dimensional features, and comparative experiments were conducted to verify the impact of dimensionality reduction on performance. Hyperparameter tuning adopts grid search, with a focus on optimizing the learning rate and the optimal value, ensuring stable convergence was finally selected.

4.5 Power consumption evaluation standard

The system's power consumption in different states was calculated using specific formulas. In standby mode, the consumption (P) is the sum of the MCU's standby power ($P_{\mathrm{MCU,standby}}$) and the power management integrated circuit (PMIC) static power ($P_{\mathrm{PMIC,quiescent}}$), as shown in Eq. (3)

$$P = P_{\mathrm{MCU,standby}} + P_{\mathrm{PMIC,quiescent}} \tag{3}$$

During motion monitoring, the power consumption includes the MCU's operational power ($P_{\mathrm{MCU,work}}$) and the impedance matching and filtering circuit's power ($P_{\mathrm{I\&F}}$), as shown in Eq. (4)

$$P = P_{\mathrm{I\&F}} + P_{\mathrm{MCU,work}} \tag{4}$$

Since we used the self-powered triboelectric sensor, the system power consumption under the scheme of using commercial IMU (P_{IMU}) and Bluetooth ($P_{\mathrm{MCU,BLE}}$) to transmit raw data can be evaluated by Eq. (5)

$$P = P_{\mathrm{IMU}} + P_{\mathrm{MCU,BLE}} \tag{5}$$

The values of $P_{\mathrm{MCU,standby}}$, $P_{\mathrm{PMIC,quiescent}}$, and P_{IMU} can be found in the datasheet. For the power $P_{\mathrm{I\&F}}$, $P_{\mathrm{MCU,work}}$, and $P_{\mathrm{MCU,BLE}}$ of the module, we designed a discrete evaluation board. Each module has an independent power supply bus, and a high-precision ammeter is connected to the power supply line to measure voltage and current (Fig. S42 in the ESM). Detailed calculation procedures for the data presented in the manuscript are provided in Note S6 in the ESM.

4.6 Characterization

The experimental test setup included a key tester, electrometer, data acquisition card, and computer. The load applicator (WP-AJ180, Shenzhen Weipin Instrument Co., Ltd.) served as a dynamic test platform for evaluating the triboelectric sensor's electrical performance under various pressures (Fig. S43 in the ESM). Open-circuit voltage and short-circuit transferred charge were measured using an electrometer (6514, Keithley) with an input impedance of 200 TΩ and recorded by a data acquisition card (DAQ 1608, National Instrument) and then transmitted to the computer. Field emission scanning electron microscopy (Gemini SEM 500, Zeiss) was utilized to analyze the material morphologies and surface microstructures of the friction and conductive layers. The elemental analysis was performed using field-emission SEM (FESEM) equipped with EDS module using Al Kα as the X-ray source.

Electronic Supplementary Material: Supplementary material (additional SEM characterizations, experimental data, experimental instructions, and other relevant information) is available in the online version of this article at https://doi.org/10.26599/NR.2026.94908328.

Data availability

All data needed to support the conclusions in the paper are presented in the manuscript and the Electronic Supplementary Material. Additional data related to this paper may be requested from the corresponding author upon request.

Acknowledgements

This work was supported by the National Natural Science Foundation of China (Nos. 52422505 and 12274124) and the Shanghai Pilot Program for Basic Research (No. 22TQ1400100-6).

Declaration of competing interest

All the contributing authors report no conflict of interests in this work.

Author contribution statement

F. Z. X., B. W. Z., and X. F. W. supervised the project. X. Z. L. conceived the idea and designed the whole project. G. Y. W. did the main work, with help from X. Z. L. and Y. Q. W. for theoretical analysis and program development. G. Y. W., X. Z. L., and Y. Q. W prepared the figures. G. Y. W., X. Z. L., Y. Q. W., and X. F. W. wrote the paper. All the authors commented on the manuscript. All the authors have approved the final manuscript.

Use of AI statement

None.

References

[1] Wang, Z. H.; Wang, S. L.; Lan, B. L.; Sun, Y.; Huang, L. C.; Ao, Y.; Li, X. L.; Jin, L.; Yang, W. Q.; Deng, W. L. Piezotronic sensor for bimodal monitoring of achilles tendon behavior. *Nano-Micro Lett.* **2025**, *17*, 241.

[2] Pu, X.; Zhang, C.; Wang, Z. L. Triboelectric nanogenerators as wearable power sources and self-powered sensors. *Natl. Sci. Rev.* **2023**, *10*, nwac170.

[3] Chen, S. W.; Fan, S. C.; Qiao, Z.; Wu, Z. X.; Lin, B. B.; Li, Z. J.; Riegler, M. A.; Wong, M. Y. H.; Opheim, A.; Korostynska, O. et al. Transforming healthcare: Intelligent wearable sensors empowered by smart materials and artificial intelligence. *Adv. Mater.* **2025**, *37*, 2500412.

[4] Lee, Y.; Gao, W. Non-invasive hormone monitoring with a wearable sweat biosensor. *Nat. Rev. Bioeng.* **2025**, *3*, 190–191.

[5] Yang, Y. D.; Chen, Y.; Liu, Y.; Yin, R. Programmable and scalable embroidery textile resistive pressure sensors for integrated multifunctional smart wearable systems. *Adv. Fiber Mater.* **2025**, *7*, 574–586.

[6] Duan, S. S.; Lin, Y. C.; Shi, Q. F.; Wei, X.; Zhu, D.; Hong, J. L.; Xiang, S. X.; Yuan, W.; Shen, G. Z.; Wu, J. Highly sensitive and mechanically stable MXene textile sensors for adaptive smart data glove embedded with near-sensor edge intelligence. *Adv. Fiber Mater.* **2024**, *6*, 1541–1553.

[7] Zhong, S. J.; Lu, B. H.; Wang, D. C.; Arianpour, B.; Wang, S. L.; Han, H. Y.; Yin, J. Y.; Bao, H.; Liu, Y. N.; Wen, Z. et al. Passive isothermal flexible sensor enabled by smart thermal-regulating aerogels. *Adv. Mater.* **2025**, *37*, 2415386.

[8] Yao, C. J.; Liu, S. H.; Liu, Z. J.; Huang, S.; Sun, T. C.; He, M. Y.; Xiao, G. M.; Ouyang, H.; Tao, Y.; Qiao, Y. C. et al. Deep learning-enhanced anti-noise triboelectric acoustic sensor for human–machine collaboration in noisy environments. *Nat. Commun.* **2025**, *16*, 4276.

[9] Fu, C. J.; Rong, C.; Zhang, B. W.; Xuan, F. Z. High-sensitivity omnidirectional recognition strain sensor based on two-dimensional materials. *Nano Res.* **2024**, *18*, 94907411.

[10] Wu, Z. F.; Huang, Y. Z.; Wang, L.; Wang, X. G.; Tan, T. N. A comprehensive study on cross-view gait based human identification with deep CNNs. *IEEE Trans. Pattern Anal. Mach. Intell.* **2017**, *39*, 209–226.

[11] Boroujeni, S. P. H.; Razi, A.; Khoshdel, S.; Afghah, F.; Coen, J. L.; O'Neill, L.; Fule, P.; Watts, A.; Kokolakis, N. M. T.; Vamvoudakis, K.

G. A comprehensive survey of research towards AI-enabled unmanned aerial systems in pre-, active-, and post-wildfire management. *Inform. Fusion* **2024**, *108*, 102369.

[12] Du, Y.; Shen, P. H.; Liu, H. F.; Zhang, Z. W.; Ren, T. L.; Shi, R.; Wang, Z. L.; Wei, D. Conformal self-powered inertial displacement sensor with geometric optimization for *in situ* noninvasive data acquisition. *Adv. Funct. Mater.* **2024**, *34*, 2409602.

[13] Jin, Y. Q.; Zhang, W. A.; Shi, L. Learning to estimate probabilistic attitude via matrix Fisher distribution with inertial sensor. *Inform. Fusion* **2025**, *119*, 103001.

[14] Wu, H.; Li, C.; Zhao, P. X.; Zhu, L. F.; Li, Y. T.; Ghomi, E. R.; Cao, H. L.; Zhang, M. Y.; Weng, X. X.; Zhang, Q. L. et al. DNA-like double-helix wrinkled flexible fibrous sensor with excellent mechanical sensibility for human motion monitoring. *Adv. Fiber Mater.* **2025**, *7*, 1260–1273.

[15] Guo, J. L.; Zhang, T. Y.; Hao, X. Y.; Liu, S. J.; Zou, Y. X.; Li, J. J.; Wu, W.; Chen, L. M.; Liu, X. Q. Aramid nanofiber/MXene-reinforced polyelectrolyte hydrogels for absorption-dominated electromagnetic interference shielding and wearable sensing. *Nano-Micro Lett.* **2025**, *17*, 271.

[16] Shang, J.; Ma, X. X.; Zou, P. K.; Huang, C. X.; Lao, Z. C.; Wang, J. H.; Jiang, T. S.; Fu, Y. Z.; Li, J. B.; Zhang, S. X. et al. A flexible catheter-based sensor array for upper airway soft tissues pressure monitoring. *Nat. Commun.* **2025**, *16*, 287.

[17] Xie, D. D.; Chen, Z. W.; Qian, D. X.; Shi, J.; Zhang, W.; Morikawa, H.; Zhu, C. H. Cat-vibrissa-inspired biomass fiber aerogels for flexible and highly sensitive sensors in monitoring human sport. *Adv. Funct. Mater.*, in press, DOI: 10.1002/adfm.202512177.

[18] Wang, D. K.; Li, B.; Niu, S. C.; Han, Z. W.; Ren, L. Q. Novel iontronic pressure sensor coupling high sensitivity and wide-range for stiffness identification and long-distance precise motion control. *Adv. Funct. Mater.* **2025**, *35*, 2413551.

[19] Yu, D.; Zheng, Z. P.; Liu, J. D.; Xiao, H. Y.; Huangfu, G.; Guo, Y. P. Superflexible and lead-free piezoelectric nanogenerator as a highly sensitive self-powered sensor for human motion monitoring. *Nano-Micro Lett.* **2021**, *13*, 117.

[20] Lee, D.; Bae, J. Soft multimodal sensors with decoupled multimodality and minimal wiring for wearable systems. *Adv. Funct. Mater.* **2024**, *34*, 2409841.

[21] Chen, Y. Q.; Liu, J.; Li, Z. Q.; Gao, Y. L.; Gao, Y.; Wang, Y. M.; Guo, X. H.; Xuan, F. Z. PEGgel-based multimodal soft sensors capable of decoupling thermal and mechanical stimuli. *Adv. Mater. Technol.* **2024**, *9*, 2400322.

[22] Zhang, C. C.; Liu, C. Z.; Li, B.; Ma, C.; Li, X. H.; Niu, S. C.; Song, H. L.; Fan, J. H.; Zhang, T.; Han, Z. W. et al. Flexible multimodal sensing system based on a vertical stacking strategy for efficiently decoupling multiple signals. *Nano Lett.* **2024**, *24*, 3186–3195.

[23] Lee, G.; Son, J.; Kim, D.; Ko, H. J.; Lee, S. G.; Cho, K. Crocodile-skin-inspired omnidirectionally stretchable pressure sensor. *Small* **2022**, *18*, 2205643.

[24] Gao, Y. J.; Ota, H.; Schaler, E. W.; Chen, K.; Zhao, A.; Gao, W.; Fahad, H. M.; Leng, Y. G.; Zheng, A. Z.; Xiong, F. R. et al. Wearable microfluidic diaphragm pressure sensor for health and tactile touch monitoring. *Adv. Mater.* **2017**, *29*, 1701985.

[25] Li, Z. Q.; Ou, F. Y.; Zhang, Z. C.; Ning, C.; Wang, F. Q.; Xie, T.; Pan, W. Y.; Zhang, Z.; Liang, Q. H.; Zhao, S. L. et al. Inspired by adipose tissue, mechanically robust and reprocessable LM-based composites for ultra-sensitive flexible pressure sensors. *Compos. Sci. Technol.* **2025**, *262*, 111061.

[26] Zhao, S. F.; Hu, F. X.; Shi, Z. Z.; Fu, J. J.; Chen, Y.; Dai, F. Y.; Guo, C. X.; Li, C. M. 2-D/2-D heterostructured biomimetic enzyme by interfacial assembling $Mn_3(PO_4)_2$ and MXene as a flexible platform for realtime sensitive sensing cell superoxide. *Nano Res.* **2021**, *14*, 879–886.

[27] Yoo, Y. J.; Heo, S. Y.; Kim, Y. J.; Ko, J. H.; Mira, Z. F.; Song, Y. M. Functional photonic structures for external interaction with flexible/wearable devices. *Nano Res.* **2021**, *14*, 2904–2918.

[28] Jin, Y.; Xue, S. A.; He, Y. Flexible pressure sensors enhanced by 3D-printed microstructures. *Adv. Mater.* **2025**, *37*, 2500076.

[29] Li, P.; Lang, S. P.; Xie, L.; Zhang, Y.; Gou, X.; Zhang, C.; Dong, C. H.; Li, C. B.; Yang, J. Skin-inspired ultra-linear flexible iontronic pressure sensors for wearable musculoskeletal monitoring. *Nano-Micro Lett.* **2026**, *18*, 55.

[30] Liu, S.; Qing, W.; Zhang, J. C.; Liao, S. H.; Wang, Q.; Wei, K. X.; Yan, W. Y.; Zhao, L. C.; Zou, H. X. Hierarchical rGO-based triboelectric sensors enable motion monitoring and trajectory tracking. *Adv. Funct. Mater.* **2025**, *35*, 2419459.

[31] Li, X. D.; Weng, M. L.; Liu, T.; Yu, K.; Zhang, S.; Ye, Z. Y.; Wang, J. L.; Liu, Y. H.; Cai, C. C.; Chi, M. C. et al. Bioinspired heterogeneous wettability triboelectric sensors for sweat collection and monitoring. *Adv. Mater.*, in press, DOI: 10.1002/adma.202509920.

[32] Ding, Q. L.; Wang, H.; Zhou, Y. B.; Zhang, Z. C.; Luo, Y. B.; Wu, Z. X.; Yang, L.; Xie, R. J.; Yang, B. R.; Tao, K. et al. Self-powered switchable gas-humidity difunctional flexible chemosensors based on smart adaptable hydrogel. *Adv. Mater.* **2025**, *37*, 2502369.

[33] Wang, Q.; Guan, H.; Wang, C.; Lei, P. M.; Sheng, H. W.; Bi, H. S.; Hu, J. K.; Guo, C. H.; Mao, Y. C.; Yuan, J. et al. A wireless, self-powered smart insole for gait monitoring and recognition via nonlinear synergistic pressure sensing. *Sci. Adv.* **2025**, *11*, eadu1598.

[34] Jang, H.; Lee, J.; Beak, C. J.; Biswas, S.; Lee, S. H.; Kim, H. Flexible neuromorphic electronics for wearable near-sensor and in-sensor computing systems. *Adv. Mater.* **2025**, *37*, 2416073.

[35] Li, Q. Y.; Gao, M. Y.; Sun, X. Q.; Wang, X. L.; Chu, D. W.; Cheng, W. L.; Xi, Y.; Lu, Y. R. All-in-one self-powered wearable biosensors systems. *Mater. Sci. Eng.: R: Rep.* **2025**, *163*, 100934.

[36] Yao, Z. Y.; Wu, W. J.; Gao, F. X.; Gong, M.; Zhang, L.; Wang, D. R.; Guo, B. C.; Zhang, L. Q.; Lin, X. Flexible tactile sensing systems: Challenges in theoretical research transferring to practical applications. *Nano-Micro Lett.* **2026**, *18*, 37.

[37] Hao, Y. J.; Hong, K. K.; Yang, J. Y.; Jia, T. Y.; Lu, X. Q.; Guo, Z.; Wang, Z. P.; Qin, Y.; Su, W.; Yang, D. et al. Evaluation and rehabilitation system for ulnar-innervated muscles facilitated by rare earth oxide-enhanced triboelectric sensor. *Adv. Mater.* **2025**, *37*, 2505613.

[38] Usman, K. A. S.; Zhang, J. Z.; Bi, L. Y.; Seyedin, S.; Wang, X. G.; Gogotsi, Y.; Razal, J. M. The future of MXene fibers. *Adv. Mater.* **2025**, *37*, 2506437.

[39] Kong, L. J.; Fang, Z.; Zhang, T. S.; Zhang, Z. T.; Pan, Y. J.; Hao, D. N.; Chen, J. F.; Qi, L. F. A self-powered and self-sensing lower-limb system for smart healthcare. *Adv. Energy Mater.* **2023**, *13*, 2301254.

[40] Sun, Y. Y.; Chen, T.; Li, D. S.; Li, H. Y.; Ji, T. C.; Wang, F. X.; Sun, L. N.; Lee, C.; Liu, H. C. Stretchable, multiplexed, and bimodal sensing electronic armor for colonoscopic continuum robot enhanced by triboelectric artificial synapse. *Adv. Mater.* **2025**, *37*, 2502203.

[41] Peng, Y. Y.; Sun, F. X.; Jing, J. H.; Zhao, J. Y.; Zhang, N.; Zhang, P. F.; Pan, R. R. Switchable pseudo-triaxial structure enabled mechanosensory textiles with ultra-wide detection range for flexible E-wearables. *Adv. Funct. Mater.* **2024**, *34*, 2411177.